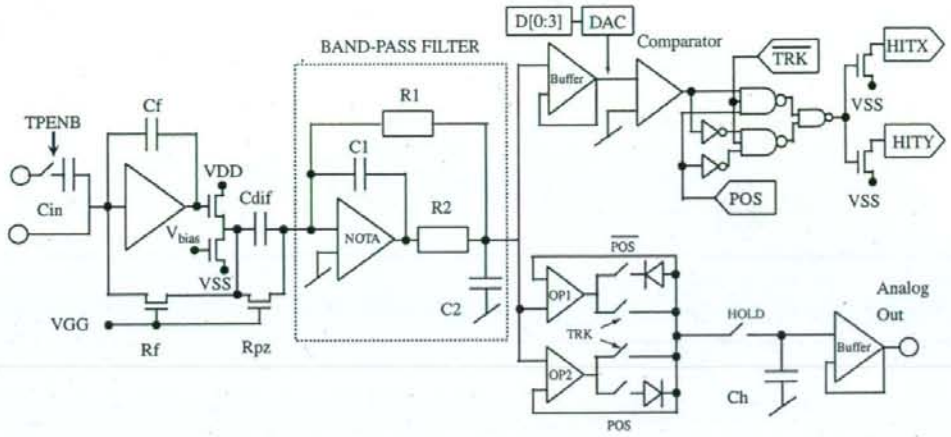

Fig. 3. Signal processing chain for each pixel cell. Here, typical values of the capacitors and resistors are $C_{in} = 0.1$ pF, $C_f = 0.02/0.04$ pF, $C_{dif} = 1.2$ pF, $C_1 = C_2 = 0.2$ pF, $R_1 = 6M\Omega$, $R_2 = 1.5M\Omega$. R_f and R_{pz} are in the range of several $M\ \Omega$ adjusted with gate voltage VGG.

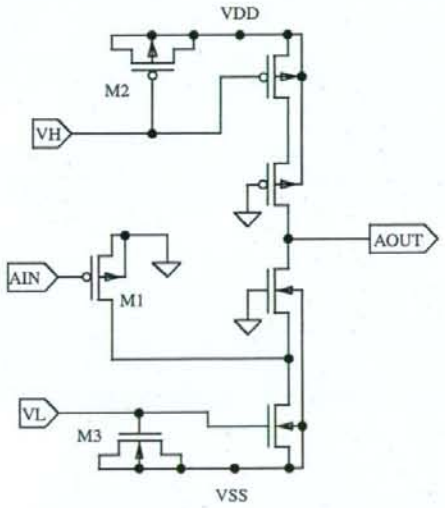

Fig. 4. Schematic of the preamplifier circuit.

conventional cascade configuration with an input PMOS transistor. We chose a PMOS transistor as an input transistor (i.e. $M1$) in terms of $1/f$ noise. In order to optimize low-noise performance, we allocated a large value of 8 μm to the gate width, and 18 to the "M value" (denoting the number of transistors arranged in parallel). The gate length is 1.8 μm. In order to maintain the low-noise characteristics, we also inserted MOS capacitors $M2$ and $M3$ to stabilize the voltage between VH and VDD, and between VL and VSS.

As shown in Fig. 3, we employed a transfer gate-type FET for the feedback component as is often used in several low-noise ASICs (see Refs. [8–13]). However, the nonlinear response of the feedback component generates waveform distortion that results in undershoot or overshoot at shaper circuit output. To eliminate undershoot, we inserted a capacitor C_{dif} and FET R_{pz} to configure a PZC circuit (e.g. Refs. [14–16]).

The architecture of the shaper circuit fundamentally adheres to that of the previously designed ASIC [6], and the shaping time constant is set at 5 μs. The output of the shaper circuit is split into the peak hold circuit and comparator circuit. The peak hold circuit consists of a peak-detect circuit and a hold circuit. In the peak-detect circuit, we employed different operational amplifiers to construct CMOS diode configurations for each polarity of the input signals. The peak-detect circuit is enabled by releasing the "TRK" signal and the peak-detect circuit output can be quickly held in a MOS capacitor by a properly timed external "HOLD" signal in concert with the comparator hit signals. The output of the peak hold circuit is fed into a multiplexer to be sequentially processed by an external A-to-D converter.

The hit signals are generated in the comparator block by referring to an analog ground level. Baseline adjustment is achieved with a current DAC controlled by signals provided by control registers. The output of the adjustment DAC is summed with the shaper circuit output and fed to the reference terminal of the discriminator.

2.3. Transfer function

The transfer function of the CSA is given as

$$T_1(s) = -\frac{R_f}{1 + sC_fR_f} \tag{1}$$

where s denotes the complex angular frequency, R_f the feedback resistance, and C_f the feedback capacitance. The PZC network shown in Fig. 3 modifies the transfer function as

$$T_1(s)' = -Q_{in}\frac{R_f}{1 + sC_fR_f}\cdot\frac{1 + sC_{dif}R_{pz}}{R_{pz}} \tag{2}$$

where C_{dif} and R_{pz} denote capacitance and resistance in the PZC circuit, respectively. By setting the parameters as

$$C_{dif}R_{pz} = C_fR_f \tag{3}$$

the "pole" associated with the signal decay of the CSA is compensated by "zero" of the PZC, and undershoot can be eliminated [17]. The above equation can be rewritten as

$$T_1(s)' = -Q_{in}\frac{C_{dif}}{C_f}. \tag{4}$$

For impedance matching, we set the M values of R_f and R_{pz}, which indicate the number of FET gates arranged in parallel, at 1:30.

The transfer function of the shaper circuit shown in Fig. 3 can be written as

$$T_2(s) = -\frac{R_1}{s^2 C_1 C_2 R_1 R_2 + sR_1 C_1 + 1}. \quad (5)$$

By setting the parameters as $C_1R_1 = 4C_2R_2$, the above equation can be rewritten as

$$-\frac{R_1}{(2sC_2R_2 + 1)^2}. \quad (6)$$

This circuit has a degenerated pole at $s = -1/2C_2R_2$ and functions as low-pass filter. Eventually the entire transfer function of the signal processing chain is given by $T_1(s)' \cdot T_2(s)$, which yields

$$Q_{in}\frac{C_{dif}}{C_f}\cdot\frac{R_1}{(2sC_2R_2 + 1)^2}. \quad (7)$$

2.4. Control scheme

Each pixel cell contains a 10-bit configuration register. Four bits are used for coarse baseline equalization (35 mV/bit), four bits for fine adjustments (5 mV/bit), one bit for masking noisy channel, and one bit to enable test pulse input. Entire bits are stored in D-type flip–flops that can be accessed by using peripheral shift registers, which also consist of D-type flip–flops and are aligned in X and Y coordinates for pixel selection. A simple protocol is used to operate configuration registers along with three control lines (for data input, write clock signals and write-enable signals). The polarity of input signals and the gain of preamplifiers ($C_f = 0.02$ or 0.04 pF) can be selected by a common setting over all the channels.

The sparse readout scheme is borrowed from the previously designed two-dimensional ASIC [5]. The readout sequence proceeds in two steps: reading the hit pattern and reading out analog outputs from selected pixels. The outputs of the comparator circuit are summed over the entire chip to be fed into an external trigger circuit. The trigger signals are also summed over row and column, with x-hit and y-hit signals being projected into the peripheral circuits to be recorded in a X–Y coordinate register for the corresponding event. Then the hit pattern is read out, the hit pixel selected, and the A-to-D conversion cycle activated according to the hit pattern.

3. Setup for performance measurements

The ASIC placed in a QFP ceramic package was held in a burn-in socket mounted on a test board. The interface with a computer was established using a National Instruments PCI-7833R board containing a reconfigurable FPGA and A-to-D converters. LabVIEW software tools were used to control the readout sequence.

4. Experimental results

4.1. Waveforms of analog outputs

We have confirmed basic operation of the ASIC by injecting test pulses and checking analog signals from the monitor outputs for 10 chips (i.e. total of 160 channels). Fig. 5 shows the outputs of the CSA and shaper circuit with three different decay time constants (C_fR_f). Test pulses equivalent to input charges of 2 fC are injected with $C_f = 0.02$ pF in each measurement. The PZC is successfully operated to suppress undershoot even if the decay time constant is comparable with the shaping time constant of the shaper circuit.

The upper and lower panels in Fig. 6 show the outputs of the shaper and peak hold circuit, respectively. The dot-dash lines indicate the SPICE simulation results. The shaper and peak hold circuits are operated properly for either positive or negative input signals. The shaping times are a bit longer than the simulation and a small overshoot is observed. The difference of the shaping times comes from a variation in resistance values of R_1 and R_2 in Fig. 3. Since the high-resistance circuits for the shaper include a 20 kΩ polysilicon resistor [6], the effective resistance value suffers from a semiconductor process variation and results in a longer shaping time. As for the small undershoot, the waveform of the SPICE simulation does not show any significant overshoot for a relative fluctuation of C_f, C_{dif} in Eq. (2), and VGG. One possible interpretation comes from interferences between the monitor line of the shaper output and the input pad of the CSA. However, our application does not require high counting rate and these influences can be negligible.

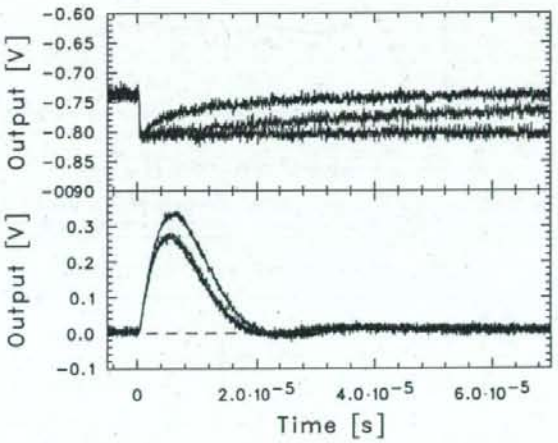

Fig. 5. Measured analog waveform traces of the outputs of the CSA and shaper circuit. The injected charges were 2 fC.

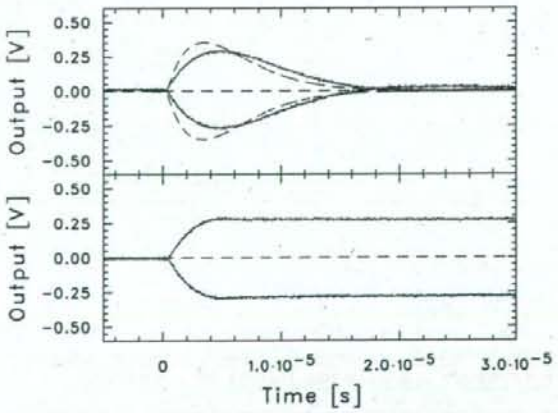

Fig. 6. Measured analog waveform traces of the outputs of the shaper and peak hold circuits. The dot-dash lines indicate the SPICE simulation results. The injected charges were 2 fC.

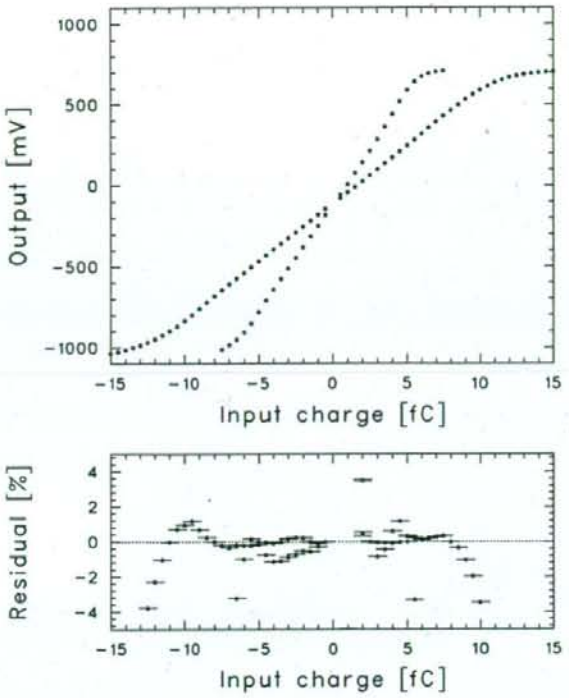

Fig. 7. Linearity curve of a typical channel. The measured data points (red: $C_f = 0.02$ pF, blue: $C_f = 0.04$ pF) are shown. The lower plots indicate the residuals between the data points and linear functions.

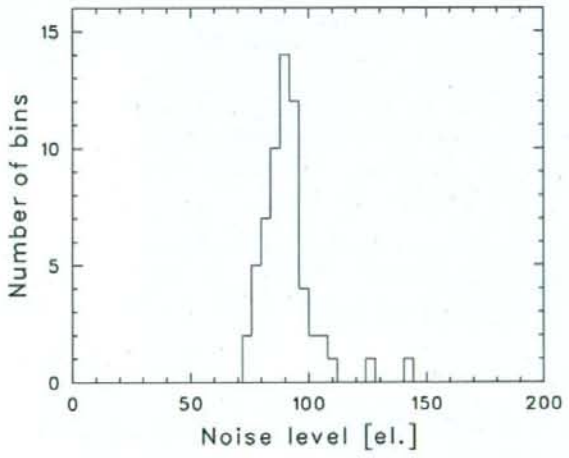

Fig. 8. Equivalent noise distribution.

4.2. Linearity and dynamic range

Fig. 7 shows the linearity curves of a typical channel. The configuration settings are the same for both negative and positive input signals. The lower panel shows the residuals between the measured data points and linear functions. Different linear functions are used for calculating the residuals between positive and negative polarities. Except for a small range of positive input charges, good linearity is maintained with an integral nonlinearity

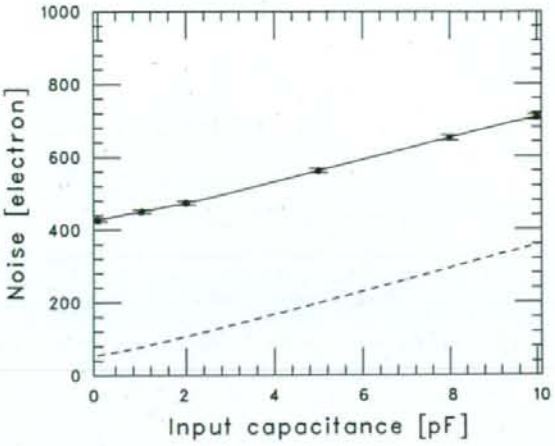

Fig. 9. Input capacitance versus equivalent noise level. The dot line shows results from a circuit simulation.

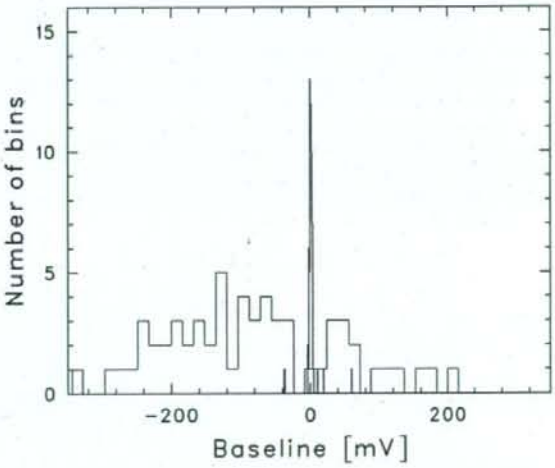

Fig. 10. Baseline distributions before and after adjustment.

of 1% in a range of −6 to +5 fC with $C_f = 0.02$ pF, while in a range of −12 to +9 fC with $C_f = 0.04$ pF.

4.3. Noise performance

Fig. 8 shows the equivalent noise distribution for input capacitance of 0 pF. Electronic noise is normalized by the response to a test pulse. The injected charge was −2 fC with the feedback capacitor of 0.02 pF. We used 12 isolated channels per chip over a total of five chips for the measurement. The mean noise level is $88 \pm 7.6e^-$ (rms) with power consumption of 150 μW per pixel, while the theoretically expected noise level is $48e^-$ (rms). The noise performance highly improved from the previously designed ASIC [6], however, there is still some room for noise improvement in the experimental setup. The current ASIC assembled in a ceramic package is tested with a burn-in socket and exposed in an exogenous noise environment. The ESD protection circuit at the input node of the CSA is removed in this design to eliminate possible origin of noise source. Since the capacitance of the CdTe

pixel detector is about 1 pF per pixel, the total noise level will satisfy our noise requirement of less than $100e^-$.

We measured the noise slope using the outer four channels connected to a DIP socket mounted on the test board. Fig. 9 shows the input capacitance versus noise level (ENC). Although the noise slopes are nearly consistent with the simulation results, the curves have excess noise of $380e^-$. That excess noise does not originate from parasitic noise due to an assembly issue. It turns out that the wiring trace for the pixel to the bonding pad capacitively introduces positive feedback to the CSA input and then, it results in circuit oscillation.

4.4. Baseline distribution

Fig. 10 shows the distribution of the output baselines. We adjusted the baselines to analog ground level to confirm the baseline adjustment range. Except for a few channels, the baseline distribution after applying the baseline adjustment is 1.66 mV, which is comparable with noise fluctuation.

5. Summary

We developed a low-noise, 16-channel two-dimensional amplifier array with TSMC 0.35-μm CMOS technology in the Open-IP LSI project for future use in hard X-ray astronomy. The entire chip consists of 4×4 matrix of identical $270\,\mu m \times 270\,\mu m$ pixel cells, each of which includes a charge-sensitive amplifier, shaper, comparator, and peak hold circuit. In the preliminary test of the ASIC, the mean equivalent noise level reached $88e^- + 25e^-/pF$ (rms) with power consumption of 150 μW per pixel. Except the pixel size, the analog performances satisfy our noise requirement of less than $100e^-$ with a detector capacitance of 1 pF, and power limits of 200 μW per pixel. In the following step, we will bump the ASIC with a CdTe pixel detector and evaluate its spectroscopic properties.

Since the circuit designs are developed in each function block, we can easily apply these circuit architectures to multi-channel ASICs for X-ray and gamma-ray imaging applications. This easy-to-use expandability supported by the good performance levels of the ASIC will lead to more applications in addition to astrophysical ones, including medical and industrial applications.

Acknowledgments

The authors would like to express their sincere gratitude for the financial support of JAXA with regards to the Steering Committee of Space Engineering. T. Kishishita is supported by research fellowships of the Japan Society for the Promotion of Science for Young Scientists.

References

[1] T. Takahashi, K. Makishima, Y. Fukazawa, M. Kokubun, K. Nakazawa, M. Nomachi, H. Tajima, M. Tashiro, Y. Terada, New Astron. 48 (2004) 269.
[2] H. Ikeda, Nucl. Instr. and Meth. A 569 (2006) 98.
[3] K. Tamura, T. Hiruta, H. Ikeda, H. Inoue, T. Kiyuna, Y. Kobayashi, K. Nakazawa, T. Takashima, T. Takahashi, IEEE Trans. Nucl. Sci. NS-52 (2004) 2023.
[4] T. Hiruta, K. Tamura, H. Ikeda, K. Nakazawa, T. Takashima, T. Takahashi, Nucl. Instr. and Meth. A 565 (2006) 258.
[5] T. Kishishita, H. Ikeda, K. Tamura, T. Hiruta, K. Nakazawa, T. Takashima, T. Takahashi, Nucl. Instr. and Meth. A 578 (2007) 218.
[6] T. Kishishita, H. Ikeda, T. Kiyuna, K. Tamura, K. Nakazawa, T. Takahashi, Nucl. Instr. and Meth. A 580 (2007) 1363.
[7] T. Kishishita, H. Ikeda, T. Kiyuna, H. Yasuda, K. Tamura, T. Takahashi, Jpn. J. Appl. Phys. 47 (5) (2008) 3423.
[8] E. Beuville, K. Borer, E. Chesi, E.H.M. Heijne, P. Jarron, B. Lisowski, S. Singh, Nucl. Instr. and Meth. A 288 (1990) 157.
[9] O. Toker, S. Masciocchi, E. Nygård, A. Rudge, P. Weilhammer, Nucl. Instr. and Meth. A 340 (1994) 572.
[10] E. Nygård, P. Aspell, P. Jarron, P. Weilhammer, K. Yoshioka, Nucl. Instr. and Meth. A 301 (1991) 506.
[11] P. Aspell, R. Boulter, A. Czermak, P. Jalocha, P. Jarron, A. Kjensmo, W. Lange, E. Nygard, A. Rudge, O. Toker, M. Turala, H. Von Der Lippe, U. Walz, P. Weilhammer, K. Yoshioka, Nucl. Instr. and Meth. A 315 (1992) 425.
[12] G.D. Geronimo, P. O'Connor, J. Grosholz, IEEE Trans. Nucl. Sci. NS-47 (2000) 1857.
[13] W.R. Cook, J.A. Burnham, F.A. Harrison, Proc. SPIE 3445 (1998) 347.
[14] G. De Geronimo, P. O'Connor, IEEE Trans. Nucl. Sci. NS-47 (2000) 1458.
[15] P. Grybos, R. Szczygiel, IEEE Trans. Nucl. Sci. NS-55 (2008) 583.
[16] C. Fiorini, M. Porro, Nucl. Instr. and Meth. A 568 (2006) 101.
[17] C.H. Nowlin, J.L. Blankenship, Rev. Sci. Instr. 36 (1965) 1830.

DRAFT VERSION MARCH 30, 2009
Preprint typeset using LaTeX style emulateapj v. 04/20/08

SUZAKU OBSERVATIONS OF EXTREME MEV BLAZAR SWIFT J0746.3+2548

SHIN WATANABE[1,2], RIE SATO[1], TADAYUKI TAKAHASHI[1,2], JUN KATAOKA[3], GREG MADEJSKI[4], MAREK SIKORA[5], FABRIZIO TAVECCHIO[6], RITA SAMBRUNA[7], ROGER ROMANI[4], PHILIP G. EDWARDS[8,1] AND TAPIO PURSIMO[9]

Draft version March 30, 2009

ABSTRACT

We report the *Suzaku* observations of the high luminosity blazar SWIFT J0746.3+2548 (J0746) conducted in November 2005. This object, with $z = 2.979$, is the highest redshift source observed in the *Suzaku* Guaranteed Time Observer (GTO) period, is likely to show high gamma-ray flux peaking in the MeV range. As a result of the good photon statistics and high signal-to-noise ratio spectrum, the *Suzaku* observation clearly confirms that J0746 has an extremely hard spectrum in the energy range of 0.3–24 keV, which is well represented by a single power-law with a photon index of $\Gamma_{\rm ph} \simeq 1.17$ and Galactic absorption. The multiwavelength spectral energy distribution of J0746 shows two continuum components, and is well modeled assuming that the high-energy spectral component results from Comptonization of the broad-line region photons. In this paper we search for the bulk Compton spectral features predicted to be produced in the soft X-ray band by scattering external optical/UV photons by cold electrons in a relativistic jet. We discuss and provide constraints on the pair content resulting from the apparent absence of such features.

Subject headings: galaxies:active, quasars:individual (J0746.3+2548), X-rays:galaxies

1. INTRODUCTION

Blazars are a sub-category of Active Galactic Nuclei (AGN) whose jet emission is pointing close to our line of sight (e.g., Urry & Padovani 1995; Ulrich, Maraschi & Urry 1997). Generally, the overall spectra of blazar sources (plotted in the $\log(\nu)$-$\log(\nu F_\nu)$ plane, where F_ν is the observed spectral flux energy density) have two pronounced continuum components: one peaking between IR and X-rays and the other in the γ-ray regime (see, e.g., Kubo et al. 1998; Ghisellini et al. 1998). The lower energy component is believed to be produced by the synchrotron radiation of relativistic electrons accelerated within the outflow, while inverse Compton (IC) emission by the same electrons is most likely responsible for the formation of the high energy γ-ray component. The spectral energy distributions (SEDs) of blazars form a sequence in luminosity, with more luminous sources having both peaks at lower energies than their fainter counterparts (Fossati et al. 1998; Ghisellini et al. 1998). In this sequence, flat-spectrum radio quasars (FSRQs) are the most luminous objects. It is widely believed, in addition, that the IC emission from FSRQs is dominated by the scattering of soft photons external to the jet (external Compton process, ERC). Those photons, in turn, are produced by the accretion disk, and interact with the jet either directly or indirectly, after being scattered or reprocessed in the broad-line region (BLR) or a dusty torus (see, e.g., Dermer & Schlickeiser 1993; Sikora et al. 1994). Other sources of seed photons can also contribute to the observed IC component; in particular, those can be the synchrotron photons themselves, radiating via the synchrotron self-Compton (SSC) process (Sokolov & Marscher 2005). In FSRQs, the synchrotron emission peaks around IR frequencies, and thus the nonthermal X-ray emission is relatively weak compared to that of other types of blazar sources. These spectral features suggest that FSRQs are well-suited for searching for the bulk Compton (BC) spectral component, which is produced by Comptonization of external UV radiation by cold electrons in a jet (Begelman & Sikora 1987; Sikora & Madejski 2000; Moderski et al. 2004; Celotti, Ghisellini & Fabian 2007). Using *Suzaku* data of PKS1510−089, Kataoka et al. (2008) argued that the observed soft X-ray excess below 1 keV and the plausible one at ~ 18 keV may be such bulk-Compton features produced by inhomogeneities prior to their collision and shock formation (the latter being the site of particle acceleration and production of the nonthermal radiation).

SWIFT J0746.3+2548 (J0746) was identified with an optically faint quasar at $z = 2.979$ detected in the 15–200 keV energy band the Burst Alert Telescope (BAT; Barthelmy et al. 2005) on board the *Swift* satellite. Its broadband spectrum is representative of other FSRQs, which have two continuum components: one peaking at IR wavelengths and the other at MeV energies. This qualifies J0746 as a likely new member of the MeV blazar class (Sambruna et

Electronic address: watanabe@astro.isas.jaxa.jp
[1] Institute of Space and Astronautical Science/JAXA, Sagamihara, Kanagawa 229-8510, Japan
[2] Department of Physics, University of Tokyo, Bunkyo, Tokyo, 113-0033, Japan
[3] Department of Physics, Tokyo Institute of Technology, Meguro, Tokyo, 152-8551, Japan
[4] Kavli Institute for Particle Astrophysics and Cosmology, Stanford University, Stanford, CA 94305, USA
[5] Nicolaus Copernicus Astronomical Center, Bartycka 18, 00-716, Warsaw, Poland
[6] INAF-Osservatorio Astronomico di Brera, Via Bianchi 46, I-23807, Merate (LC), Italy
[7] NASA Goddard Space Flight Center, Greenbelt, MD 20771, USA
[8] Australia Telescope National Facility, CSIRO, Locked Bag 194, Narrabri NSW 2390, Australia
[9] Nordic Optical Telescope, Apdo 474, 38700 Santa Cruz de La Palma, Spain

al. 2006). The X-ray spectrum observed by *Swift* XRT was hard in the 0.5–8 keV with a photon index $\Gamma_{\rm ph} \sim 1.3$. Moreover, *Swift* data showed spectral hardening at energies <1 keV, which Sambruna et al. (2006) interpreted as an excess absorption over the Galactic value, or a flatter power-law component, implying a sharp ($\Delta\Gamma_{\rm ph} \sim 1.1$) spectral break at ~4 keV. It has been argued that a clear distinction between the two possibilities can be made by *Suzaku*, due to its broad bandpass, good photon statistics and low background data.

In 2005 November, simultaneous observations were performed with the Very Large Array (VLA; radio), the 26 m diameter University of Michigan Radio Astronomy Observatory (UMRAO; radio), the 14 m diameter Metsähovi radio-telescopes (radio), the Hobby-Eberly Telescope (HET; optical), the 2.56m Nordic Optical Telescope(NOT; optical), *Swift* XRT and UVOT (optical-UV, X-ray) and *Suzaku* (X-ray). Sambruna et al. (2006) presented some of the simultaneous observations in addition to the description of J0746 discovery with *Swift*. In this paper, we report a detailed analysis of the ~ 100 ks *Suzaku* observation of J0746 as a part of the SWG (science working group) program. Moreover, we present the multiband analysis using all simultaneous observations. This paper is organized as follows. In §2, we described the *Suzaku* observation and data reduction. In §3, we report the optical and radio results, which were not reported in Sambruna et al. (2006). In §4, we present the spectral analysis of the *Suzaku* X-ray data as well as multiband analysis. Finally, we discuss the constraints on the content of the jet inferred from the X-ray spectrum in §5. Throughout this paper, we adopt the cosmological parameters $H_0 = 71$ km s^{-1} Mpc^{-1}, $\Omega_{\rm M} = 0.27$ and $\Omega_\Lambda = 0.73$.

2. SUZAKU OBSERVATION AND DATA REDUCTION

2.1. *Observation*

J0746 was observed with *Suzaku* (Mitsuda et al. 2007) from 2005 November 4 at 08:20 UT until November 6 14:04 UT, during the performance verification (PV) phase. Table 1 summarizes the start and end times, and the exposures of the *Suzaku* observation (sequence number 700011010). *Suzaku* has four sets of X-ray telescopes (Serlemitsos et al. 2007) each with a focal-plane X-ray CCD camera (X-ray Imaging Spectrometer(XIS); Koyama et al. 2007) that are sensitive in the energy range of 0.3–12 keV. Three of the XIS (XIS 0, 2, 3) detectors have front-illuminated (FI) CCDs, while the XIS 1 utilizes a back-illuminated (BI) CCD. The merit of the BI CCD is its improved sensitivity in the soft X-ray energy band below 1 keV. *Suzaku* also features a non-imaging collimated Hard X-ray Detector (HXD; Takahashi et al. 2007), which covers the 10–600 keV energy band with Si PIN photodiodes and GSO scintillation detectors. *Suzaku* has the two default pointing positions, XIS nominal position and HXD nominal position. In this observation, we used the HXD nominal position, in which the effective area of the HXD is maximized, whereas that of the XIS is reduced to ~ 88% on the average.

2.1.1. *XIS Data Reduction*

The XIS data used in this paper were version 1.2 of the cleaned data. The screening is based on the following criteria: (1) ASCA-grade 0, 2, 3, 4, and 6 events were accumulated, and the CLEANSIS script was used to remove hot or flickering pixels, (2) data collected within 256 s of passage through the South Atlantic Anomaly (SAA) were discarded, and (3) data were selected to be 5° in elevation above the Earth rim (20° above the day-Earth rim). After this screening, the net exposure for good time intervals is 100.5 ksec.

The XIS events were extracted from a circular region with a radius of 2.6′ centered on the source peak, whereas the background was accumulated in an annulus with inner and outer radii of 2.6′ and 4.3′, respectively. The response (RMF) files used in this paper are the standard RMF files (ae_xi{0,1,2,3}_20060213.rmf), provided by the XIS instrumental team. The auxiliary (ARF) files are produced using the analysis tool XISSIMARFGEN developed by the *Suzaku* team, which is included in the software package HEAsoft version 6.2.

2.1.2. *HXD/PIN Data Reduction*

The PIN source spectra were extracted from cleaned version 1.2 HXD/PIN event files. Data were selected according to the following criteria: (1) More than 500 s from a South Atlantic Anomaly passage, (2) cut-off rigidity above 8 GV, and (3) day- and night-Earth elevation angles each 5°. After this screening and the dead time correction using "pseudo-events" (Kokubun et al. 2007), the net exposure for good time intervals becomes 74.0 ksec.

The PIN spectrum is dominated by the time-variable instrumental background induced by cosmic-rays and trapped charged particles in the satellite orbit. The HXD instrument team has developed an effective method (Watanabe et al. 2007) of modeling the time-dependent non-X-ray background (NXB) by making use of the PIN upper discriminator (UD) signal that monitors passing charged particles through the silicon PIN diode. The background spectrum is generated based on a database of NXB observations accumulated to date during night- and day-earth observations. The current NXB model is shown to be accurate within ~ 4%. (Mizuno et al. 2006).

Another component of the HXD PIN background is the Cosmic X-ray background (CXB). The form of the CXB was taken as 9.0×10^{-9}(E/3 keV)$^{-0.29}$exp(−E/40 keV) erg cm^{-2} s^{-1} (Gruber et al. 1999). The CXB spectrum observed with HXD/PIN was simulated by using a PIN response file for isotropic diffuse emission (ae_hxd_pinflat_20060809.rsp). However, Kokubun et al. (2007) reported that the PIN returns a ~13–15% larger normalization than the XIS based on the most recent calibration using the Crab Nebula. Additionally, it was reported that the XIS normalization of the Crab Nebula agrees with the conventional Crab Nebula flux derived from previous satellites. Therefore, we introduced a scaling factor of 1.13 to normalize the CXB spectrum.

We used the response files version ae_hxd_pinxinom_20060814.rsp, provided by the HXD instrumental team. As reported in Kokubun et al. (2007), the response file returns 15% larger flux at the HXD nominal position pointing than the XIS flux. Therefore, we corrected the normalization of the HXD/PIN in the spectral analysis (§3.2).

Figure 1 shows the time averaged HXD/PIN spectrum. The NXB model, the CXB model and the 4% level of the NXB are also plotted in the spectrum. The hard X-ray emission of J0746 was detected in the energy range from 12 keV to 24 keV, assuming the 4% accuracy of the current NXB model. Above 24 keV, the upper limit of flux could be derived from the accuracy of the NXB model. We also note here that the source was not detected in the GSO data.

3. OPTICAL AND RADIO OBSERVATIONS

3.1. *Hobby-Eberly Telescope (HET)*

The optical spectra were obtained with the 9.2m Hobby-Eberly telescope (HET; Ramsey et al. 1998) Marcario Low Resolution Spectrograph (LRS; Hill et al. 1998). Observations were made from 2005 November 5 to November 6 covering λ420–1000 nm at 1.6 nm resolution. The seeing was variable during the integrations and so spectrophotometry was not attempted. However, observations were taken with the slit along the parallactic angle and at constant air mass and, using white-light pre- and post- spectrum direct images, indicating that the source faded by 0.17 magnitudes between the observations. Using this information, we correct for the differential slit losses, adjusting the first (worse-seeing) spectrum to that of November 6. The resulting spectra are shown in Figure 2, after standard calibrations and correction for an estimated Galactic extinction of E(B−V)=0.07.

Overall, the spectra do not differ dramatically from the spectrum of the blazar available from the SDSS archive. However, there is clearly a fading component in the continuum. In the first spectrum, a power-law fit to the continuum to the red of Lyα gives $F_\nu = 6.6 \times 10^{-28}(\nu/10^{14.7}\mathrm{Hz})^{-0.8}\mathrm{erg/cm^2/s/Hz}$; during the second observation the continuum flux was $F_\nu = 5.6 \times 10^{-28}(\nu/10^{14.7}\mathrm{Hz})^{-0.6}\mathrm{erg/cm^2/s/Hz}$, the residual slit losses leave a $\sim$ 10% uncertainty in the absolute fluxes. The broad-line flux is, as expected, nearly constant on this timescale, confirming the relative spectral normalization estimated from the direct images. The difference spectrum between the two epochs is nearly pure continuum, with a spectral index of $\alpha \sim 2$–2.5, suggesting that a fading synchrotron component is contributing to the optical flux during the tail of the outburst. These two observations were obtained only a month after the observations reported by Sambruna et al. (2006), conducted on 2005 October 10 - also with the LRS on the HET - reported by Sambruna et al. (2006), and the continuum flux (at 6500 angstrom) is about twice of the average of the two of our flux measurements taken in November 2005.

3.2. *Nordic Optical Telescope (NOT)*

We carried out the photometric observations of J0746 at the 2.56 m Nordic Optical Telescope (NOT) at La Palma (Observatorio del Roque de los Muchachos, Canary Islands) on 2005 November 5 using ALFOSC (Andalucia Faint Object Spectrograph and Camera). The data have been reduced using the "standard" IRAF procedures (de-biasing and flat-fielding were applied for all images) and the magnitudes were measured using IRAF/apphot-package. The magnitudes of the object and the comparison stars were measured using a relatively small aperture (about the size of the seeing disc) and the final brightness of the object via differential photometry. In order to flux calibrate the comparison stars, the magnitudes were measured using a large aperture (19″diameter). The brightnesses of the comparison stars were determined using two different techniques: (1) using the published SDSS g'and r' magnitudes and transforming these magnitudes to V and R, respectively, (2) using Landolt standard stars (PG2213−006 and Mark_A) (Landolt 1992) observed earlier the night having about the same airmass as the target. Galactic extinction was corrected by using Schlegel, Finkbeiner & Davis (1998). The R-band and the V-band photometric measurements were made with an exposure of 200 seconds. The R-band and V-band fluxes of J0746 were 18.9 and 19.2 magnitudes, respectively. The detailed results are given in Table 2.

3.3. *The Very Large Array (VLA)*

We observed J0746 with the Very Large Array (VLA) between 11:25 and 13:25 UT on 2005 November 3, at the end of the reconfiguration period from DnC array to D array. In D configuration, the most compact array, the maximum baseline is 1.03 km. A total of 22 antennas were available for the observations, which were made at 1.425, 4.860, 8.460, 14.940, 22.460 and 43.340 GHz. 3C138 (J0521+1638) was used as the primary flux density calibrator. J0746 was observed in three blocks, with each block containing a ∼170 second scan at each frequency. Between each block, a similar block of observations of 3C138 was carried out, using scans of 100 seconds. The 15, 22 and 43 GHz scans, for both J0746 and 3C138, were preceded by a 270 second pointing scan on source at 8 GHz to determine a pointing offset for the higher frequencies, following the standard VLA reference pointing procedure.

The data were amplitude calibrated in AIPS using the scans on 3C138 to set the flux density scale. At the three highest frequencies the source models for 3C138, supplied with the data, were used. After amplitude calibration the data were written out and read into `Difmap`. After initial phase self-calibration, the data were modeled by a point source. Inspection of the correlated flux density as a function of (u, v) distance confirmed this assumption was valid at all frequencies for J0746 in this array configuration. The individual scans were also independently model-fit, but no evidence for significant variability over the ∼2 hour period was apparent. The results are given in Table 3.

The 1.4 GHz flux density is almost 10% less than measurements from ∼10 years earlier in the NVSS (Condon et al. 1998) and FIRST (Becker et al. 1995) catalogs, however the 4.9 GHz flux density is significantly higher than the 0.48±0.04 Jy in the GB6 (Gregory et al. 1996) catalog. The inverted spectrum between 1.4 and 4.9 GHz, α =0.56 ($S \propto \nu^{+\alpha}$ suggests the presence of strong self-absorption at the lowest frequency. Above 4.9 GHz the spectral index is −0.40, although the 15 GHz and, to a lesser extent, 22 GHz flux densities deviate from a single spectral index fit.

4. ANALYSIS AND RESULTS

4.1. *Temporal analysis*

Figure 3 shows the averaged light curves of the XIS/FIs in three energy bands: 0.5–2 keV (*upper* panel), 2–10 keV (*middle* panel), and total (0.5–10 keV; *bottom* panel), respectively. Since the count rate variations of the HXD/PIN detector were less clear due to limited photon statistics and uncertainly of the NXB modeling, in the following we concentrate on the temporal variability of the XIS data only, below 10 keV. Figure 4 compares the count-rate correlation between the soft X-ray (0.5–2 keV) and the hard X-ray energy bands (2–10 keV). We can see that there is no significant correlation between the soft X-ray flux and the hard X-ray flux, which indicates that the variability in the soft and hard X-ray bands are not well synchronized. Although *Suzaku* X-ray light curve shows some variability, it is not nearly as strong as that measured by *Swift*, where Sambruna et al. (2006) reported that the *Swift* XRT detected a factor of ~ 2 flux change in a few hours. We try to evaluate the variability by calculating the variability amplitude relative to the mean count rate corrected for effects of random errors (e.g., Edelson et al. 2002): $F_{\rm var} = 1/\overline{x}\sqrt{S^2 - \overline{\sigma_{\rm err}}^2}$, where S^2 is the total variance of the light curve, $\overline{\sigma_{\rm err}}^2$ is the mean error squared and $\overline{x}$ is mean count rate. The variability amplitude of J0746 is $F_{\rm var,soft} \sim 0.033 \pm 0.018$ and $F_{\rm var,hard} \sim 0.026 \pm 0.013$, and the energy-dependence of variability is flat.

4.2. *Spectral Analysis*

The XIS and HXD/PIN background subtracted spectra were fitted using XSPEC v11.3.2, including data within the energy range 0.3–24 keV. The Galactic absorption toward J0746 is taken to be $N_H = 4.04 \times 10^{20}$ cm^{-2} (Dickey & Lockman 1990). Note that our best-fitting value for the column density, $N_H = (4.89 \pm 0.50) \times 10^{20}$ cm^{-2} (Table 4), which is approximately consistent with the Galactic value and there is no significant excess absorption. All errors are quoted at the 68.3% (1σ) confidence level for the parameters. The fits are restricted to the energy range 0.5–10 keV (XIS 0, 2, 3: FI chips), 0.3–7 keV (XIS 1: BI chip) and 11–24 keV (HXD/PIN), respectively. In the following analysis, we fixed the relative normalization of the XISs and PIN at 1.15 (see § 2.1.1).

Figure 5 (*left*) shows four XISs and HXD/PIN background-subtracted spectra with residuals to the power-law with the Galactic column density, determined using the data from 0.3 keV to 24 keV (model 1). We obtained the photon index of $\Gamma_{\rm ph}$=1.17, but this model did not represent the spectra well yielding a χ^2/dof of 1238/1112. Some scatter in the residual panel in Figure 5 (*left*) indicates that the spectral normalization among the XISs is not constant. To represent the shape of the observed X-ray spectra, we adjusted the normalization factor among the four XISs relative to XIS 0 (model 2). Since Serlemitsos et al. (2007) reported that the spectral normalizations are slightly (a few percent) different among the CCD sensors based on the contemporaneous fit of the Crab spectra, the few percent adjustment of the relative normalization is reasonable. This model well reproduced the spectra with the best χ^2/dof of 1113/1109 (Figure 5: *right*). For this model the photon index is $\Gamma_{\rm ph} = 1.18$ with Galactic absorption, and the 2–10 keV flux of XIS0 is $(3.07 \pm 0.03) \times 10^{-12}$ erg cm^{-2} s^{-1}. This corresponds to the *Swift* XRT flux of $\sim 3 \times 10^{-12}$ erg cm^{-2} s^{-1}. All of the spectral fitting results are summarized in Table 4. We conclude that the X-ray spectra of J0746 within the energy range 0.3–24 keV are well described by an extremely hard power-law ($\Gamma_{\rm ph} = 1.17$) with the Galactic absorption.

4.3. *Spectral energy distribution*

Figure 6 shows the spectral energy distribution (SED) of J0746 during the 2005 November campaign. Blue and red represent simultaneous data of the radio, UV, optical and X-ray observations. Historical data taken from radio (NED), and γ-ray (EGRET upper limit; Sambruna et al. 2006) observations are also plotted in cyan and black, respectively. Figure 6 implies that the synchrotron component of J0746 most likely peaks around $\sim 10^{11} - 10^{12}$ Hz in the observer frame. Meanwhile, *Swift* UVOT data show the steep optical-UV emission as the high-energy tail of the "blue bump" which is thought to be produced via thermal emission by the accretion disk and/or corona near the central black hole of J0746 (Sun & Malkan 1989). Apparently, these optical-UV data do not join smoothly with the X-ray-to-γ-ray spectrum, which is likely due to the nonthermal External Compton jet radiation (ERC) or due to synchrotron-self-Compton emission (SSC) (e.g., Ballo et al. 2002).

In order to model the SED of J0746, we applied the synchrotron-inverse Compton (IC) emission model described in Maraschi & Tavecchio (2003), where both synchrotron and external photons are considered as seed radiation fields contributing to the IC process. The electron distribution is modeled as a smoothed broken power-law;

$$n_e(\gamma) = K\gamma^{-n_1}\left(1 + \frac{\gamma}{\gamma_{\rm brk}}\right)^{n_1 - n_2}, \quad (1)$$

where K (cm^{-3}) is a normalization factor, n_1 and n_2 are the spectral indices below and above the break Lorentz factor $\gamma_{\rm brk}$. The electron distribution extends within the limits $\gamma_{\rm min} < \gamma < \gamma_{\rm max}$.

We assume that the blazar radiation originates in a region located at a distance r from the black hole, well within the Broad Line Region but sufficiently far above the accretion disk that the radiation energy density from the latter can be neglected. The external radiation field can then be simply modeled,

$$U_{\rm diff} \simeq \frac{L_{\rm BLR}}{4\pi r_{\rm BLR}^2 c}, \quad (2)$$

where $r_{\rm BLR}$ is the size of the broad-line-region.

Figure 6 shows the best-fit model for J0746 data, combining of the synchrotron, the SSC, and the ERC components (Tavecchio & Ghisellini 2008), plus the blue bump emission. The spectrum can be completely fitted with the model parameters; the emission region is modeled as a sphere with radius $R = 3.2 \times 10^{16}$ cm moving with a bulk Lorentz factor $\Gamma = 20$ at an angle $\theta = 0.05$ rad between the line of sight and the jet axis, and filled by tangled magnetic field $B = 1.8$ G and relativistic electrons. The Doppler beaming factor is $\delta \equiv 1/[\Gamma(1 - \beta\cos\theta)] \sim 20$. Parameters of the electron distribution are $n_1 = 1.34$, $n_2 = 3.8$, $\gamma_{\rm min} = 1$, $\gamma_{\rm brk} = 27$, $\gamma_{\rm max} = 10^3$, respectively. The size of the BLR is assumed to be $r_{\rm BLR} = 6.5 \times 10^{17}$ cm, and the luminosity of broad emission lines $L_{\rm BLR} = 2 \times 10^{45}$ ergs s^{-1}. The disk blue bump has a luminosity $L_{\rm disk} \simeq 1.8 \times 10^{47}$ ergs s^{-1} and temperature $kT_{\rm UV} = 10$ eV (redshifted temperature 2.5 eV).

5. DISCUSSION

5.1. *Suzaku results of J0746*

In previous sections, we presented temporal and spectral analysis of *Suzaku* observation of J0746 in 2005 November. Using the high-sensitivity, broadband instruments onboad *Suzaku*, we found the following characteristics of J0746: (1) The variability amplitude of soft (0.5–2 keV) and hard (2–10 keV) bands are both $F_{\rm var,soft} \sim F_{\rm var,hard} \simeq 0.03$. There seems to be no significant energy-dependence of the variability. (2) The observed X-ray spectrum is well-described by a hard power-law ($\Gamma_{\rm ph} = 1.17$) with the Galactic absorption. Thanks to the good photon statistics and spectral response of *Suzaku* XIS, we clearly confirmed that J0746 has an intrinsically hard spectrum and can exclude the possibility that the spectral hardening results from the excess absorption as reported by Sambruna et al. (2006). Such differences of the spectrum between *Swift* and *Suzaku* are probably due to (1) low statistics of *Swift* XRT compared to *Suzaku*, and (2) Sambruna et al. (2006) combining the X-ray spectra obtained at 4 different epochs, with different exposures. The observed photon index is extremely hard, similar to those observed in several high-luminosity blazars (e.g., Tavecchio et al. 2000). As long as the X-ray emission is due to the low-energy end of the ERC spectral component, the observed photon index $\Gamma_{\rm ph} = 1.17$ corresponds to the electron distribution $n_e(\gamma) \propto \gamma^{-1.34}$, where γ is the Lorentz factor of the ultrarelativisitic electrons. A likely explanation of such a flat electron distribution is discussed by Sikora et al. (2002) who assume a two-step acceleration process: the harder portion is produced by a pre-acceleration mechanism, e.g., involving instabilities driven by shock-reflected ions (Hoshino et al. 1992) or magnetic reconnection (Romanova & Lovelace 1992), while the high energy tail by the standard first-order Fermi process operating over the shock front.

5.2. *Constraint on Bulk Compton emission*

As the cold electrons/positrons, before reaching the blazar dissipative site, are transported from the black hole vicinity by a jet with a bulk Lorentz factor $\Gamma_{\rm jet} \sim 10$–20, they upscatter the accretion disk and broad emission line photons to energies

$$h\nu_{\rm BC,obs} \simeq \Gamma_{\rm jet}\delta_{\rm jet} h\nu_{\rm diff}/(1+z) \tag{3}$$

where $h\nu_{\rm diff} \sim 10$ eV. This is expected to produce a hump in the X-ray spectra of blazars with luminosity

$$L_{BC} \simeq N_e |dE_e/dt|(\delta_{\rm jet}^3/\Gamma_{\rm jet}) \simeq \frac{4}{3}\sigma_T U_{BLR} r_{BLR} \dot{N}_e \Gamma_{\rm jet}\delta_{\rm jet}^3, \tag{4}$$

where $|dE_e/dt| = (4/3)c\sigma_T U_{BLR}\Gamma_{\rm jet}^2$ and $N_e \simeq \dot{N}_e r_{BLR}/c$ is the number of electrons enclosed in the jet within a distance range corresponding with the scale of the broad emission line region.

For our observation of J0746, the soft X-ray excess which would indicate the BC feature is not detected. However, since the *Suzaku* observation of J0746 was performed in a relatively low state with an average flux of $F_{2-10{\rm keV}} \sim 3 \times 10^{-12}$ erg cm^{-2} s^{-1}, we can put a stringent upper limit on the BC emission. The limit is presented in Figure 7. It is obtained using *Suzaku* data fitted with power-law determined in § 4.2 plus black-body approximation of the bulk-Compton component. As an example, a comparison between the model and the data is shown in Figure 8, and, some of the fitting results are also listed in Table 4 (model 3-1 and model 3-2). In Figure 7, the marked 'allowed region' corresponds with a temperature range $kT = 0.40$–1.0 keV which, in turn, corresponds with $\Gamma_{\rm jet} = \delta_{\rm jet} \sim 10$–$20$. In this region the upper limit of BC luminosity is $L_{\rm BC} \leq 6.6 \times 10^{45}$ erg s^{-1} .

It should be noted here that in the case of the popular internal shock model (e.g., Spada et al. 2001) the bulk-Compton radiation is produced by two cold inhomogeneities/shells. In this case production of any nonthermal flare by the internal shock should be proceded by a pair of X-ray precursors: one produced by a faster shell at larger energies and lasting shorter; and one produced by a slower shell at lower energies and lasting longer. Radiative bulk-Compton features from such systems are very complex, are variable and depend on the model details (Moderski et al. 2004). However, a small amplitude of variability in J0746 (see Figure 3) suggests that if the primary dissipative events are driven by internal shocks, what we observe is an overlap of radiation contributed by several shocks. Then the upper limits for the bulk-Compton emission calculated using the 'steady state' may be a reasonable approximation.

5.3. *Constraint on particle content in the jet of J0746*

Noting that the energy flux carried by the cold electrons is

$$L_{e,\rm cold} \simeq n_e m_e c^3 \Gamma_{\rm jet}^2 \pi R_{\rm jet}^2 \equiv \dot{N}_e m_e c^2 \Gamma_{\rm jet}, \tag{5}$$

where $R_{\rm jet}$ is the cross-section radius of a jet, one can find after combining Eq. (4) and Eq. (5) that

$$L_{\rm BC} \simeq \frac{4\sigma_{\rm T}}{3m_e c^2}\, U_{\rm BLR}\, r_{\rm BLR}\, \delta_{\rm jet}^3\, L_{\rm e,cold}. \tag{6}$$

For the upper limit for $L_{\rm BC}$ given by *Suzaku* data (see § 5.2) this gives

$$L_{\rm e,cold} \leq 1.0\times10^{44} \left(\frac{r_{\rm BLR}}{6.5\times10^{17}\ {\rm cm}}\right) \left(\frac{\delta_{\rm jet}}{20}\right)^{-3} \left(\frac{L_{\rm BLR}}{1.8\times10^{45}\ {\rm erg\ s^{-1}}}\right)^{-1} {\rm erg\ s^{-1}}. \tag{7}$$

Meanwhile, the ERC modeling of J0746 presented in the previous section (§ 4.3) implies the jet power carried by the ultrarelativisitic (non-thermal, or 'hot') electrons $L_{\rm e,hot} \simeq \dot{N}_e m_e c^2 \bar{\gamma}_e \Gamma_{\rm jet} \sim 4\times10^{45}$ erg s^{-1}, where $\bar{\gamma}_e$ is the average random Lorentz factor of electrons/positrons. However, if a jet is free of protons and the only source of the energy is the bulk energy of cold pairs, then from the energy conservation one can deduce that $L_{\rm e,hot} < L_{\rm e,cold}$. This is in a clear disagreement with the obtained upper limit for $L_{\rm e,cold}$ and the model value of $L_{\rm e,hot}$.

Such situation may be avoided if one assumes that there are cold protons which carry significant power $L_p > L_{\rm e,hot} \gg L_{\rm e,cold}$. In this case $L_{\rm e,hot}/(L_{\rm e,cold}+L_{\rm p,cold}) \lesssim 1$, and, provided that jet kinetic luminosity $L_{\rm jet} \simeq L_{\rm p,cold}$, the pair content reads as

$$\frac{n_e}{n_p} = \frac{m_p}{m_e}\frac{L_{\rm e,cold}}{L_{\rm p,cold}} \simeq \frac{m_p}{m_e}\frac{L_{\rm e,cold}}{L_{\rm jet}}. \tag{8}$$

Noting that the luminosity of the observed high energy (γ-ray) emission can be related to the jet kinetic luminosity via the relation $L_\gamma \simeq \eta_\gamma(\delta_{\rm jet}^3/\Gamma_{\rm jet})L_{\rm jet}$, where η_γ is the efficiency of the high energy γ-ray production, we finally find that the upper limit for the pair content of the J0746 jet is

$$\frac{n_e}{n_p} \leq 7.3\times \left(\frac{\eta_\gamma}{0.1}\right) \left(\frac{r_{\rm BLR}}{6.5\times10^{17}\ {\rm cm}}\right) \left(\frac{\Gamma_{\rm jet}}{20}\right)^{-1} \left(\frac{L_{\rm BLR}}{1.8\times10^{45}\ {\rm erg\ s^{-1}}}\right)^{-1} \left(\frac{L_\gamma}{10^{48}\ {\rm erg\ s^{-1}}}\right)^{-1}. \tag{9}$$

For J0746, we only have an upper limit on the gamma-ray flux of $L_\gamma \sim 10^{48}$ erg s^{-1}. With this, and $L_{\rm BLR} \sim 1.8\times10^{45}$ erg s^{-1}, we obtained $n_e \leq 7.3\ (\eta_\gamma/0.1)\ n_p$. This may indicate a rather low pair content in quasar jets. However, it should be noted that J0746 has an exceptionally hard X-ray spectrum. For blazars with softer X-ray spectra a lack of bulk-Compton features put weaker constraints, $n_e/n_p \leq$ tens, But the inertia of such jets is still dominated by protons (Sikora & Madejski 2000).

6. SUMMARY

We have presented a detailed analysis of *Suzaku* observation for the radio-loud quasar J0746 at $z = 2.979$ in 2005 November. Our results are the following:

1. The variability amplitude of soft and hard bands as measured by *Suzaku* is equivalent and there is no significant energy-dependence of the variability, in contrast to the much larger (factor of 2) variability reported from the Swift data.

2. The observed X-ray spectrum of J0746 is well-described by a single, extremely hard power-law ($\Gamma_{\rm ph} = 1.17$) with the Galactic absorption; we do not require spectral hardening at the lowest energies seen by Sambruna et al. (2006). With this, we can exclude excess absorption (which would otherwise have to be rapidly variable!) to cause the spectral hardening, one of the possibilities considered by Sambruna et al. (2006).

3. A lack of bulk Compton features in the X-ray spectra indicates a low electron-positron pair content and strong dominance jet inertia by protons.

We thank the anonymous referee for her/his valuable comments that helped to improve this paper.

The National Radio Astronomy Observatory (NRAO) is a facility of the National Science Foundation operated under cooperative agreement by Associated Universities, Inc. NRAO is thanked for the provision of Target of Opportunity time for the observations, and Barry Clark is thanked for assistance is the preparation of observing files. The research described here we supported in part by the Department of Energy contract to SLAC no. DE-AC3-76SF00515, and NASA grant to Stanford University no. NNX07AB05G. Based on observations made with the Nordic Optical Telescope, operated on the island of La Palma jointly by Denmark, Finland, Iceland, Norway, and Sweden, in the Spanish Observatorio del Roque de los Muchachos of the Instituto de Astrofisica de Canarias.

REFERENCES

Barthelmy, S. D., et al. 2005, Space Sci. Rev., 120, 143
Ballo, L., et al. 2002, ApJ, 567, 50
Becker, R. H., White, R. L., & Helfand, D. J. 1995, ApJ, 450, 559
Begelman, M. C., & Sikora, M. 1987, ApJ, 322, 650
Celotti, A., Ghisellini, G., & Fabian, A. C. 2007, MNRAS, 375, 417
Condon, J. J., Cotton, W. D., Greisen, E. W., Yin, Q. F., Perley, R. A., Taylor, G. B., & Broderick, J. J. 1998, AJ, 115, 1693
Dermer, C. D., & Schlickeiser, R. 1993, ApJ, 416, 458
Dickey, J. M., & Lockman, F. J. 1990, ARA&A, 28, 215
Edelson, R., Turner, M. J. L.,Pounds, K., Vaughan, S., Markowitz, A., Marshall, H., Dobbie, P., & Warwick, R. 2002, ApJ, 568, 61
Fossati, G., Maraschi, L., Celotti, A., Comastri, A., & Ghisellini, G. 1998, MNRAS, 299, 433
Ghisellini, G., Celotti, A., Fossati, G., Maraschi, L., & Comastri, A. 1998, MNRAS, 301, 451
Gregory, P. C., Scott, W. K., Douglas, K., & Condon, J. J. 1996, ApJS, 103, 427
Gruber, D. E., Matteson, J. L., Peterson, L. E., & Jung, G. V. 1999, ApJ, 520, 124
Hill, G.J., Nicklas, H.E., MacQueen, P.J., Tejada, C. Cobos Duenas, F.J. & Mitsch, W. 1998, Proc. SPIE, 3355, 375
Hoshino, A., Arons, J., Gallant, Y. A., & Langdon, A. B. 1992, ApJ, 390, 454
Jorstad, S. G., et al. 2005, AJ, 130, 1418
Landolt, A. 1992, AJ, 104, 340
Maraschi, L., & Tavecchio, F. 2003, ApJ, 593, 667
Malkan, M. A., & Moore, R. L. 1986, ApJ, 300, 216
Mitsuda, K., et al. 2007, PASJ, 59, 1
Mizuno, T., et al. 2006, Suzaku Memo, JX-ISAS-SUZAKU-MEMO-2006-42
Moderski, R., Sikora, M., Madejski, G. M., & Kamae, T. 2004, ApJ, 611, 770
Kataoka, J., et al. 2008, ApJ, 672, 787
Kokubun, M., et al. 2007, PASJ, 59, 53
Koyama, K. et al. 2007, PASJ, 59, S23
Kubo, H., Takahashi, T., Madejski, G., Tashiro, M., Makino, F., Inoue, S., & Takahara, F. 1998, ApJ, 504, 693
Pian, E. & Treves, A. 1993, ApJ, 416, 130
Ramsey, L.W. et al. 1998, Proc. SPIE, 3352, 34
Romanova, M. M., & Lovelace, R. V. E. 1992, A&A, 262, 26
Sambruna, R., et al. 2006, ApJ, 646, 23
Spada, M., Ghisellini, G., Lazzati, D., & Celotti, A. 2001, MNRAS, 325, 1559
Schlegel, D. J., Finkbeiner, D. P., & Davis, M. 1998, ApJ, 500, 525
Serlemitsos, P. J., et al. 2007, PASJ, 59, 9
Sikora, M., Begelman, M. C., & Rees, M. J., 1994, ApJ, 421, 153
Sikora, M. & Madejski, G. M. 2000, ApJ, 534, 109
Sikora, M., Błażejowski, M., Moderski, R., & Madejski, G. M. 2002, ApJ, 577, 78
Sokolov, A., & Marscher, A.P. 2005, ApJ, 629, 52
Sun, W.-H., & Malkan, M. A. 1989, ApJ, 346, 68
Takahashi, T. et al. 2007, PASJ, 59, S35
Tavecchio, F., et al. 2000, ApJ, 543, 535
Tavecchio, F., & Ghisellini, G. 2008, MNRAS, 386, 945
Ulrich, M-H., Maraschi, L., & Urry, C. M. 1997, ARA&A, 35, 445
Urry, C. M., & Padovani, P. 1995, PASP, 107, 803
Watanabe, S., et al. 2007, Suzaku Memo, JX-ISAS-SUZAKU-MEMO-2007-01

TABLE 1
2005 SUZAKU OBSERVATION LOG OF J0746.

Start (UT)	Stop (UT)	Exposure (ks) XIS	Exposure (ks) HXD/PIN
Nov. 04 08:20 2005	Nov. 06 14:04 2005	100.5	74.0

TABLE 2
NOT PHOTOMETRIC OBSERVATIONS OF J0746.

Band	Flux (mag)	std[a]	photerr[b]	calibration[c]	exposure (second)	time (UT)
R-band	18.888	0.006	0.011	(1)	200	2005 November 5
	18.937	0.017	0.011	(2)		05:38:37
V-band	19.232	0.024	0.010	(1)	200	2005 November 5
	19.233	0.005	0.010	(2)		05:44:05

[a]Standard deviation of the target brightness estimates.
[b]The apphot error estimate for the target.
[c] (1): using the published SDSS g'r' magnitudes and transforming these magnitudes to V and R. (2): using Landolt standard stars (PG2213−006 and Mark_A).

TABLE 3
VLA OBSERVATIONS OF J0746.

Frequency (GHz)	Flux density (Jy)
1.425	0.38
4.860	0.76
8.460	0.61
14.940	0.44
22.460	0.43
43.340	0.32

TABLE 4
RESULTS OF THE SPECTRAL FITS TO THE *Suzaku* SPECTRA.

Component	Parameter	model 1	model 2	model 2′	model 3-1	model 3-2
Absorption	$N_{\rm H}$ (10^{20}cm^{-2})	4.04 (fixed)	4.04 (fixed)	4.89±0.50	4.04 (fixed)	4.04 (fixed)
Power-law	$\Gamma_{\rm ph}$	1.17±0.01	1.18±0.01	1.20±0.01	1.17 (fixed)	1.17 (fixed)
	$F_{2-10\ {\rm keV}}$ (10^{-12} erg s^{-1} cm^{-2})	3.10±0.02	3.07±0.03	3.06±0.04	3.08±0.02	3.05±0.04
Constant	XIS 0	1.00 (fixed)	1.00 (fixed)	1.00 (fixed)	1.00 (fixed)	1.00 (fixed)
	XIS 1	1.00 (fixed)	0.91±0.01	0.91±0.01	1.00 (fixed)	1.00 (fixed)
	XIS 2	1.00 (fixed)	1.04±0.01	1.04±0.01	1.00 (fixed)	1.00 (fixed)
	XIS 3	1.00 (fixed)	1.05±0.01	1.05±0.01	1.00 (fixed)	1.00 (fixed)
	HXD/PIN	1.15 (fixed)	1.15 (fixed)	1.15 (fixed)	1.15 (fixed)	1.15 (fixed)
Black-Body	Temperature (keV)	-	-	-	0.4 (fixed)	1.0 (fixed)
(Bulk-Compton)	Luminosity(10^{45} erg s^{-1})	-	-	-	0.8 (0.0–1.6)	3.9 (1.0–6.6)
χ^2/d.o.f ($\chi^2_{\rm red}$)		1238/1112 (1.11)	1113/1109 (1.00)	1110/1108 (1.00)	1238/1112 (1.11)	1237/1112 (1.11)

NOTE. — Errors correspond to 1 σ confidence level.

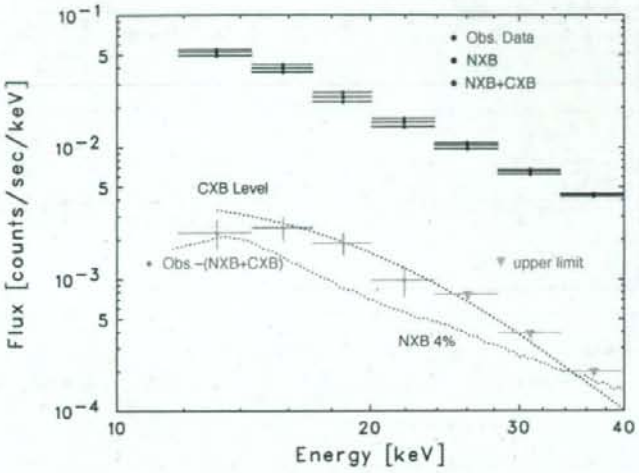

FIG. 1.— The time averaged HXD/PIN spectra. The red and the black show the observed data and the non X-ray background (NXB) model spectrum, respectively. The background model spectrum including NXB and CXB is plotted in blue. After the background subtraction, the detected spectrum and the upper limit assuming the 4% accuracy of the NXB model are plotted in green and cyan, respectively.

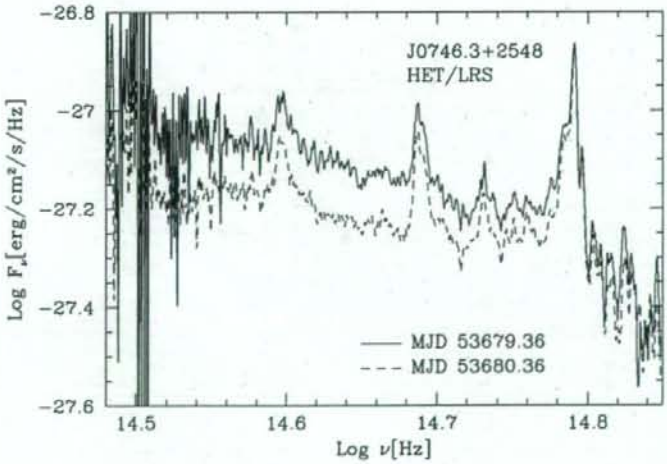

FIG. 2.— Optical spectra of J0746 during 2005 November observations.

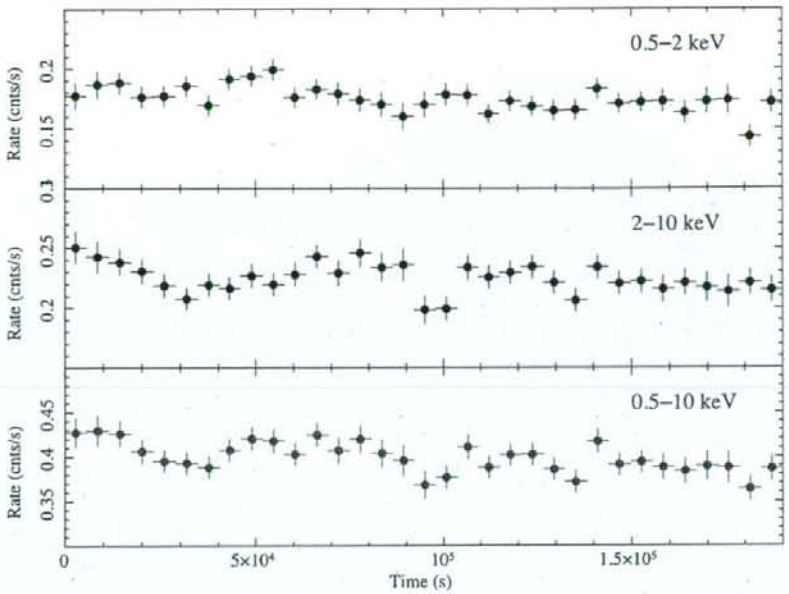

FIG. 3.— Light curves of J0746 during 2005 November observations in the three energy bands: 0.5–2 keV (*upper*), 2–10 keV (*middle*), and total 0.5–10 keV (*bottom*). All the light curves were binned at 5760 s, corresponding to the period of the Suzaku orbit.

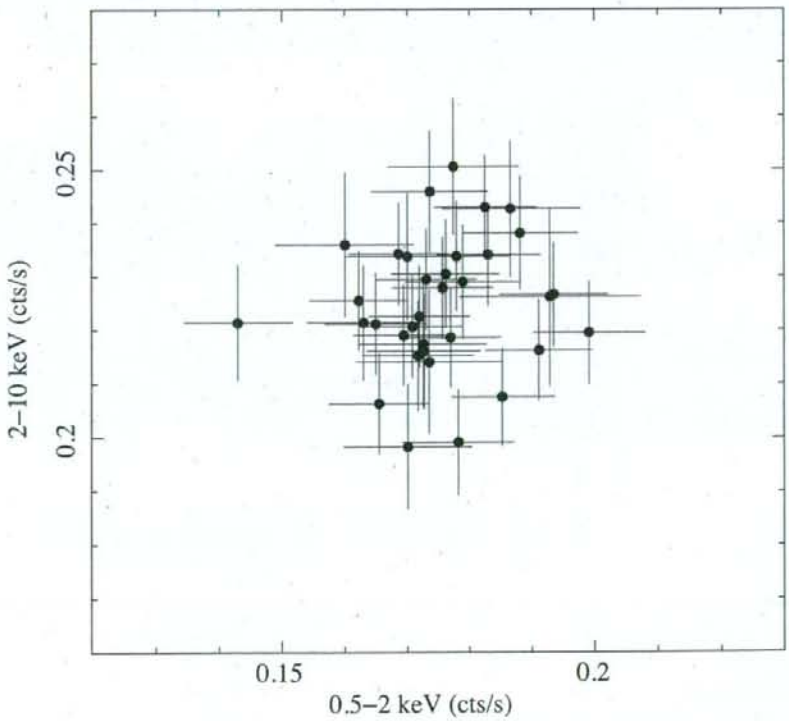

FIG. 4.— Correlation of XIS/FI count rates between 0.5–2 keV and 2–10 keV.

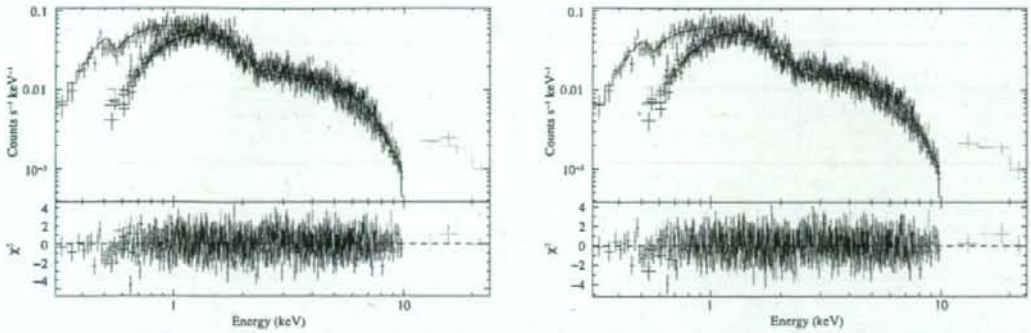

FIG. 5.— *Left*: Broadband (0.3–24 keV; XIS[0–3] + HXD/PIN) Suzaku spectra of J0746. The black, red, green and blue points show the XIS0,1,2,3 spectra, respectively. The cyan points are HXD-PIN spectrum. The upper panel shows the background subtracted spectra, plotted with an absorbed power-law model of photon index $\Gamma_{ph} = 1.17$ and a column density 4.04×10^{20} cm^{-2} (Galactic value). The lower panel shows the residuals to this power-law model fit. Some scatter in the residual panel shows that spectral normalization is not consistent. *Right*: the spectrum plotted against the best-fit model composed of an absorbed power-law with constant factors.

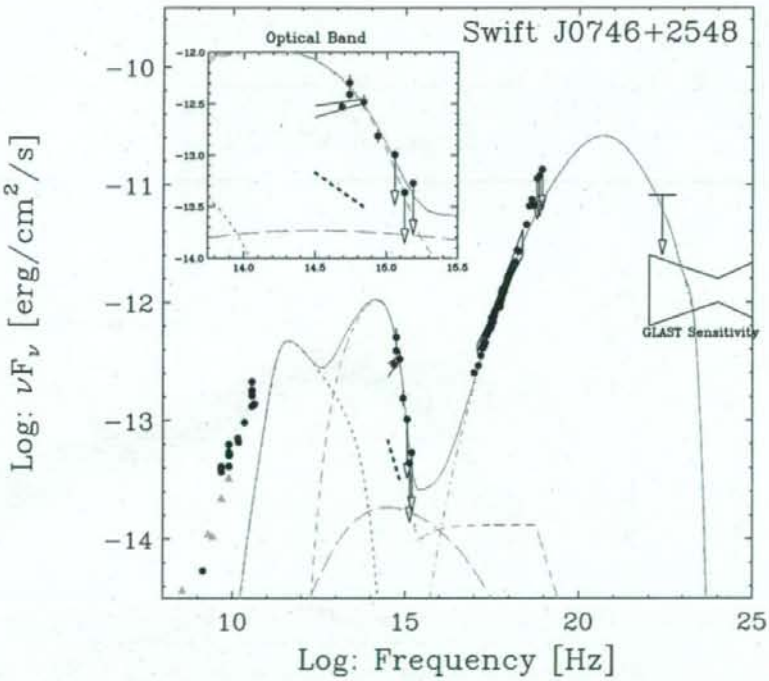

FIG. 6.— Overall SED of J0746 constructed with multiband data obtained during the November 2005 campaign (red and blue). The red filled circles and lines show the observation results presented in this paper: radio (VLA), optical-UV(NOT; filled circles and HET; lines) and X-ray (*Suzaku*). For the HET data, the difference spectrum between the two epochs is shown in the red dotted line. The blue filled circles and lines show the data presented by Sambruna et al. (2006): radio (Metsahovi and UMRAO), optical-UV (*Swift* UVOT) and X-ray (*Swift* XRT). The data plotted with cyan triangles are from NED, while the GeV upper limit shows the EGRET data analyzed by Sambruna et al. (2006). The green solid line shows the jet continuum calculated with the jet emission model described in § 4.3, as a sum of various emission components: synchrotron (dotted line), blue bump (dashed line), SSC (long dashed line) and ERC (dot dashed line). Moreover, the sensitivity of one year GLAST observation is also plotted for reference.

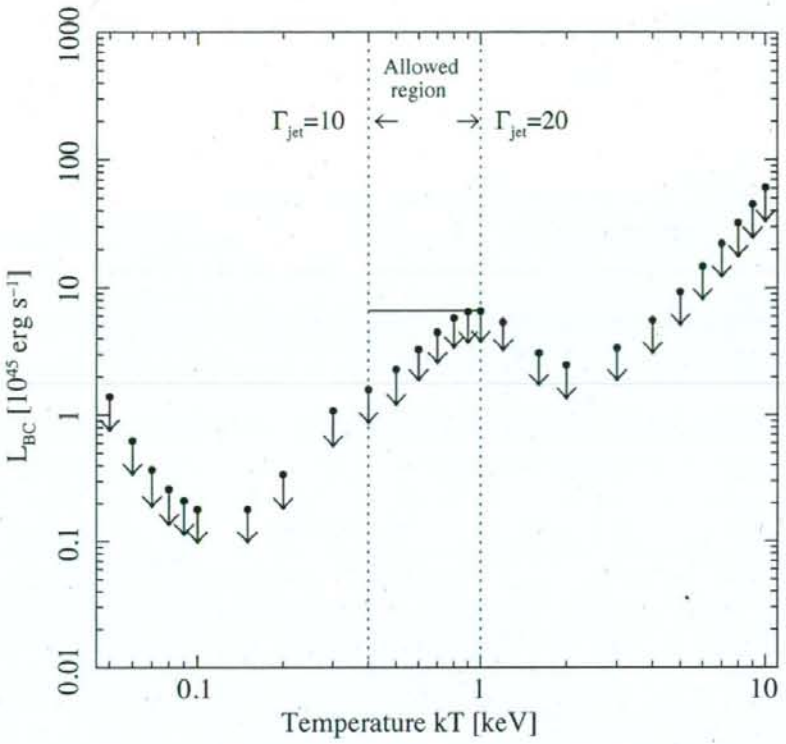

FIG. 7.— The 1 σ upper limit of the BC component luminosity estimated from *Suzaku* data fitting with power-law + black-body model.

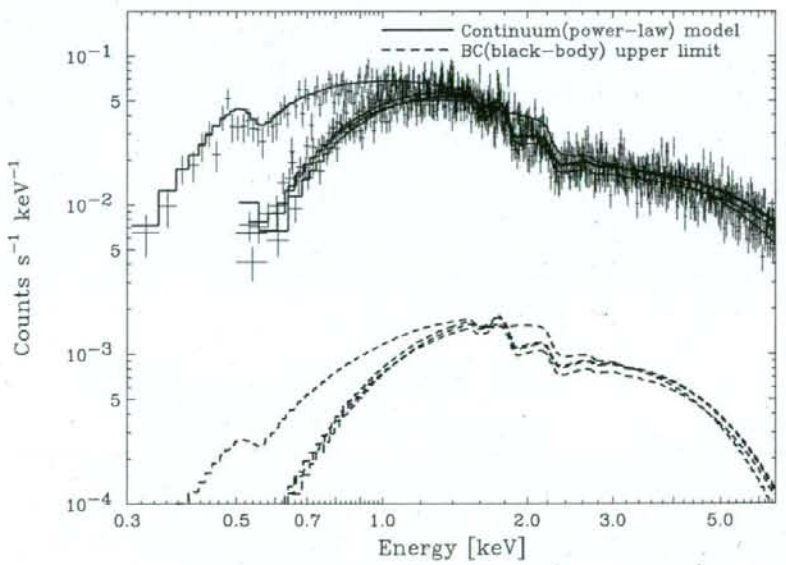

FIG. 8.— A comparison between the model (continuum + bulk Compton component) and the data. As the the bulk-Compton component, a black-body with a temperature of 1.0 keV is assumed, and the 1 σ upper limit is plotted.

High energy resolution hard X-ray and gamma-ray imagers using CdTe diode devices

Shin Watanabe, Shin-nosuke Ishikawa, Hiroyuki Aono, Shin'ichiro Takeda, Hirokazu Odaka, Motohide Kokubun, Tadayuki Takahashi, Kazuhiro Nakazawa, Hiroyasu Tajima, Mitsunobu Onishi, Yoshikatsu Kuroda

Abstract—**We developed CdTe double-sided strip detectors (DSDs or cross strip detectors) and evaluated their spectral and imaging performance for hard X-rays and gamma-rays. Though the double-sided strip configuration is suitable for imagers with a fine position resolution and a large detection area, CdTe diode DSDs with indium (In) anodes have yet to be realized due to the difficulty posed by the segmented In anodes. CdTe diode devices with aluminum (Al) anodes were recently established, followed by a CdTe device in which the Al anodes could be segmented into strips. We developed CdTe double-sided strip devices having Pt cathode strips and Al anode strips, and assembled prototype CdTe DSDs. These prototypes have a strip pitch of 400 μm. Signals from the strips are processed with analog ASICs (application specific integrated circuits). We have successfully performed gamma-ray imaging spectroscopy with a position resolution of 400 μm. Energy resolution of 1.8 keV (FWHM: full width at half maximum) was obtained at 59.54 keV. Moreover, the possibility of improved spectral performance by utilizing the energy information of both side strips was demonstrated. We designed and fabricated a new analog ASIC, VA32TA6, for the readout of semiconductor detectors, which is also suitable for DSDs. A new feature of the ASIC is its internal ADC function. We confirmed this function and good noise performance that reaches an equivalent noise charge of 110 e^- under the condition of 3–4 pF input capacitance.**

I. Introduction

HARD X-ray and gamma-ray imaging spectrometers with good spatial and energy resolutions are desired for medical, industrial and astrophysical applications. Cadmium telluride (CdTe) and cadmium zinc telluride (CZT) are very promising materials for hard X-ray and gamma-ray imaging spectrometers, given their high detection efficiency comparable to that of NaI scintillators and good energy resolution comparable to that of Ge detectors. Although both CdTe and CZT are vulnerable to energy resolution and peak detection efficiency being degraded due to their poor charge transport properties, several techniques have been developed to maintain good spectral performance [1], [2].

S. Watanabe, S. Ishikawa, H. Aono, S. Takeda, H. Odaka and T. Takahashi are with Institute of Space and Astronautical Science, Japan Aerospace Exploration Agency, Sagamihara, Kanagawa, Japan, and also with Department of Physics, University of Tokyo, Bunkyo, Tokyo, Japan.

M. Kokubun is with Institute of Space and Astronautical Science, Japan Aerospace Exploration Agency.

K. Nakazawa is with Department of Physics, University of Tokyo.

H. Tajima is with Stanford Linear Accelerator Center, Menlo Park, CA, USA.

M. Onishi and Y. Kuroda are with Nagoya Guidance and Propulsion Systems Works, Mitsubishi Heavy Industry Ltd., Komaki, Aichi, Japan.

Manuscript accepted Oct 12, 2008

CdTe/CZT semiconductor detectors require segmented readout electrodes in order to obtain position information. For imagers having a fine position resolution, there are two types of detector configurations: pixel detectors and double-sided strip detectors (Fig. 1).

A pixel detector has a number of small pixel electrodes on one side. The signal from each pixel is processed with each charge-sensitive amplifier. Since the leakage current and the detector capacitance become very small, ideal spectral performance is consequently possible. However, an extremely large number of readout channels are needed for a fine position resolution and/or large detection area. Additionally, a two-dimensional readout ASIC is essential for fine pitch pixels [3]–[5].

A double-sided strip detector (DSD or cross strip detector) realizes a fine position resolution and large detection area with a relatively small number of readout channels. The DSD has orthogonal strips implemented on both its sides. By reading out the signal from both side strips coincidentally, it is possible to obtain information on the position and energy of the X-ray/gamma-ray photons [6], [7]. The number of the readout channels is proportional to $2N$ (where N denotes the number of segments per coordinate) for DSDs, instead of N^2 for pixel detectors. Therefore, for a larger N (meaning a finer position resolution and/or larger area), the DSD has an advantage in terms of readout channels. Moreover, one-dimensional ASICs that are easier to implement and more common than two-dimensional ones are also applicable to DSDs.

Our development is aimed at hard X-ray imaging detectors for the ASTRO-H (NeXT) project that plans to launch Japan's 6th X-ray astronomy satellite in 2013. Among the major objectives is achieving high sensitivity observation with focusing and imaging capabilities in the 5–80 keV energy region. The ASTRO-H satellite will carry two hard X-ray telescopes that feature multilayer supermirrors assembled in grazing incident X-ray telescopes. Hard X-ray Imagers (the focal plane detectors of hard X-ray telescopes) require an energy resolution of $\sim$ 1 keV (FWHM: full width at half maximum), energy coverage of 5–80 keV, a sub-mm (250–500 μm) position resolution, detection area of 2–3 cm, and timing resolution of $\sim$ 1 μs for high sensitivity observation. To achieve these goals, we have developed CdTe diode DSDs as a primary choice for Hard X-ray Imagers. In this paper, we describe our development of CdTe DSDs, and report the results of the CdTe DSD prototypes. We also report on our newly developed ASIC (VA32TA6) for semiconductor detector readout.

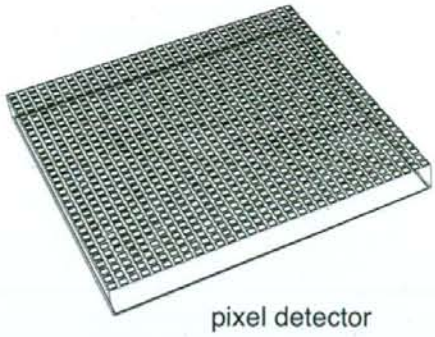

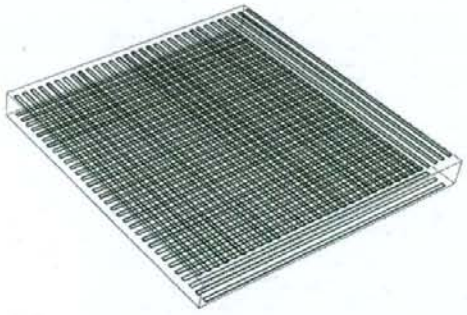

Fig. 1. Pixel detector and double-sided strip detector.

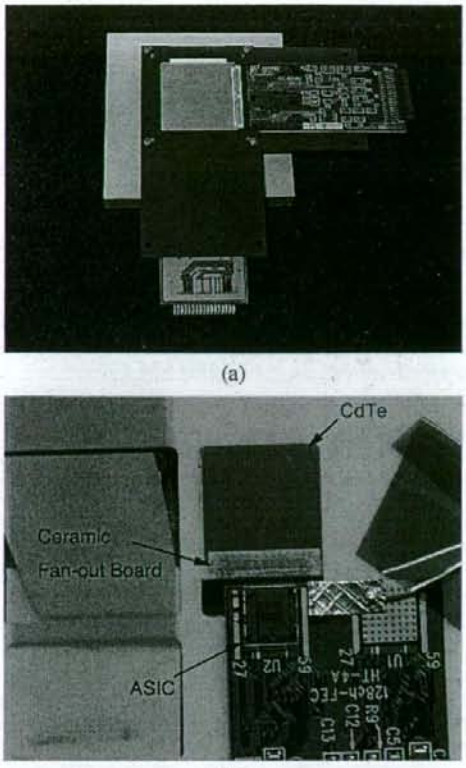

Fig. 2. Prototypes of the CdTe DSDs. (a): The 2.6 cm CdTe DSD. It is 2.6 cm × 2.6 cm in size and, 500 μm thick. The strip pitch is 400 μm. On each side 64 strips are formed, and two VA32TAs are used for readout on each side. (b): The 1.3 cm CdTe DSD. It is 1.3 cm × 1.3 cm in size, and 500 μm thick. The strip pitch is 400 μm. On each side 32 strips are formed, and one VA64TA2 is used for readout on each side.

II. Prototypes of CdTe DSDs

A. CdTe Diode Device with Double-Sided Strips

Thin CdTe diode devices that utilize indium (In) as the anode electrodes on p-type CdTe wafers manufactured by ACRORAD (Japan) and platinum (Pt) as the cathodes have been established and offer good spectral performance [1]. A high Schottky barrier formed on the In/p-CdTe interface enables use of the detector as a diode. Using this type of detector with a thickness of 0.5 mm at applied bias voltages as high as 1 kV makes it possible to overcome the poor charge transport properties of CdTe. However, double-sided strip detectors with In anodes cannot be realized since it is difficult to segment the In electrode into strips.

Aluminum (Al) has recently been found to be a good alternative electrode material to In [8], [9]. In addition to low leakage currents and high energy resolutions comparable to those of In/CdTe/Pt detectors, Al/CdTe/Pt detectors also offer the advantage of allowing Al anodes to be divided into pixels or strips. CdTe diode detectors with segmented Al anodes have been established by constructing and testing Al-pad/CdTe/Pt or Al-pixel/CdTe/Pt type detectors. Good spectral performance ($\Delta E \sim 1$ keV(FWHM) at 60 keV) has been achieved [10], [11].

By adopting segmented Al anodes and Pt cathodes, we can obtain a CdTe diode double-sided strip device. For the prototype detectors, we fabricated two types of the CdTe devices: the 2.6 cm CdTe device and 1.3 cm CdTe device. The 2.6 cm CdTe device is 2.6 cm × 2.6 cm in size, and 500 μm thick. On each side 64 strips are formed, with a strip pitch of 400 μm. Moreover, 350 μm strip electrodes and 50 μm gaps are alternately formed. The 1.3 cm CdTe device is 1.3 cm × 1.3 cm in size, and 500 μm thick. On each side 32 strips are formed. The strip pitch and electrode configuration are the same as those of the 2.6 cm CdTe DSD. Both devices have guard-ring electrodes on both sides to reduce leakage current of the strips.

B. Configurations of Prototypes

We used the CdTe double-sided strip devices described above to assemble two types of prototype CdTe DSDs: the 2.6 cm CdTe DSD and the 1.3 cm CdTe DSD. Fig. 2 shows the prototype detectors. We employed VA32TAs [12] and VA64TA2s [13] that we jointly developed with GM-IDEAS to read out the 2.6 cm and the 1.3 cm CdTe DSDs, respectively.

Given the soft and fragile characteristics of CdTe material, we have yet to establish a reliable technique of wire-bonding

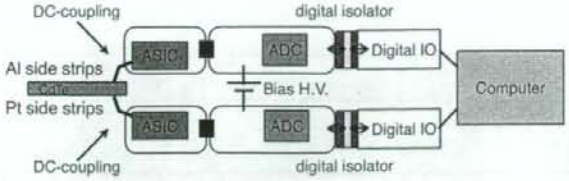

Fig. 3. Readout system of the CdTe DSDs.

on the CdTe surface. Therefore, it is difficult to interconnect the CdTe strip electrodes and the readout ASIC input pads by using wire-bonding as applied to Si DSDs [14], [15].

To overcome this problem, we adopted the In/Au stud bump bonding technique and used the Al_2O_3 ceramic fan-out board with through-holes. First, the CdTe strip electrodes are connected via In/Au stud bump bonding to the Al_2O_3 ceramic fan-out board that we developed and established for CdTe-Pixel/Pad detectors [16]. This ceramic fan-out board has through-holes to interconnect the electrodes on both sides of the fan-out board. Then, wire-bonding can be done from the ASIC input pads to the electrodes on the ceramic board. We have connected readout ASICs on both sides of the CdTe DSDs in this manner. A more detailed procedure is described in elsewhere [17].

Fig. 3 shows a block diagram illustrating the overall readout system. This system is virtually the same as the scheme implemented for the readout of Si DSDs [14], [15]. The readout ASICs and strip electrodes are connected with DC-coupling for both sides. The detector bias voltage is supplied by applying a high voltage between local grounds of the Al anodes and Pt cathodes.

C. Imaging and Spectral Performance

In order to demonstrate the imaging capability of the test devices, we took shadow images of metal objects with various gamma rays from radioisotopes such as ^{241}Am, ^{133}Ba and ^{57}Co. Fig. 4 shows the shadow images obtained with the 2.6 cm CdTe DSD and the target. The hole of a 2-mm nut and solder 0.6 mm diameter can be clearly seen. It can also be seen that a thin washer becomes transparent as the energy of gamma rays becomes higher. However, the energy resolution obtained with the 2.6 cm CdTe DSD did not match that obtained with pad-type Al anode detectors. FWHM energy resolutions of 2.6 keV and 6.2 keV at 59.54 keV were obtained for the spectra from Pt strips and Al strips, respectively, under 500 V of bias voltage and temperature of −20°C.

For a detailed study of spectral performance, we tested a 1.3 cm CdTe DSD. The smaller capacitance and lower leakage current afforded by smaller detector size should lead us to better noise performance. The spectral performance of VA64TA2 for negative signals from the Al strips has also been improved compared with VA32TA used in the 2.6 cm CdTe DSD.

Fig. 5 show the spectra obtained with the 1.3 cm CdTe DSD. Under operating conditions of −20°C temperature and 500 V of applied bias voltage, the total leakage current from all strips

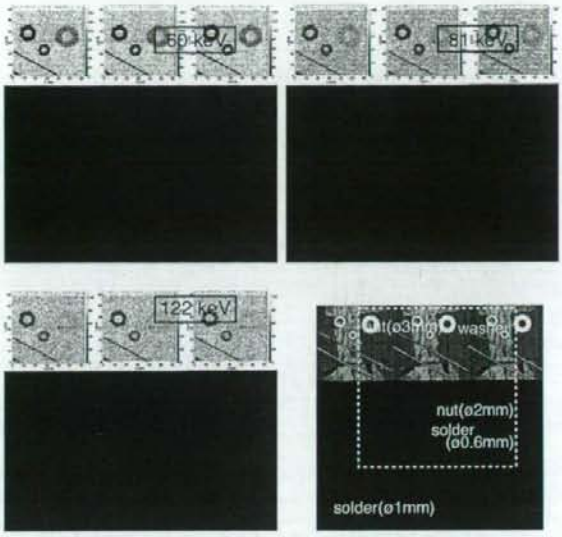

Fig. 4. Shadow images obtained with the 2.6 cm CdTe DSD and a photograph of the target. The energies of the gamma rays are 60 keV (^{241}Am), 81 keV (^{133}Ba) and 122 keV (^{57}Co). The pixel size in the images corresponds to a strip pitch of 400 μm.

and guard-rings was 5 nA. The trigger energy threshold can be set to about 10 keV. An energy resolution of 1.8 keV (FWHM) at 59.54 keV was obtained for both the Pt and Al sides. The spectral performance for the Al and Pt sides was confirmed as being equivalent in the CdTe DSDs.

By collectively using the energy information on both sides, improved spectral performance could be expected if each noise component was independent. We created a spectrum by filling the average of the both sides' energy information, as shown in Fig. 6. This spectrum shows improved energy resolution. Thus, an energy resolution of 1.4 keV (FWHM) was successfully obtained.

For imagers, uniform spectral performance in each detector is important. In the double-sided strip configuration, we can examine a kind of uniformity by sorting the events of one strip based on the position information obtained from the other side's strips. Since only one channel of the ASIC is used for the readout, we can obtain the position dependence without the effect of readout variation. Fig. 7 shows a ^{241}Am gamma-ray spectrum from one strip on the Al side. The Y axis corresponds to the hit strip on the Pt side. It can be seen that the spectrum is constant with the position. The peak position and energy resolution for 59.54 keV gamma rays were stable within 0.2% and 12%, respectively.

III. Brand New Readout ASIC, VA32TA6

We have been developing readout ASICs for our applications in collaboration with GM-IDEAS. Based on past developments, we designed and fabricated a new readout ASIC, VA32TA6. Fig. 8 shows a photograph of VA32TA6 and a schematic diagram of the ASIC. VA32TA6 is fabricated using AMS 0.35 μm technology with an epitaxial layer. The die is